Kinematic Rupture Characterization of Large Compressional Intraslab Earthquakes Along the Tohoku Region, Japan

.

K. Tsuda[1], S. Yoshida[2], C. Ji[3], R.J. Archuleta[3,4], and T. Sato[2]

[1]Institute of Technology Shimizu Corporation, Tokyo, Japan.

[2]Ohsaki Research Institute Inc., Tokyo, Japan.

[3]University of California, Santa Barbara, CA, USA.

[4]RJA Ground Motion Analysis Inc., Santa Barbara, CA, USA

Corresponding author: Kenichi Tsuda (kenichi.tsuda@shimz.co.jp)

Key Points:

- Slip histories of four Mw>7 intraslab down-dip compressional (DDC) earthquakes in the Tohoku region are estimated by finite-fault inversions.
- The source parameters of these DDC earthquakes are in agreement with the previous scaling laws for intraslab earthquakes at a similar depth.
- The recurrence intervals of these events are comparable with the ones of megathrust earthquakes similar to the 2011 Tohoku earthquakes.

Abstract

We examine the source parameters of four Mw≥7.0 intraslab earthquakes that occurred near the Tohoku coast over the past two decades: 2003, 2011, 2021, and 2022. By analyzing the finite fault slip histories constrained by inland strong motion observations, we found that these earthquakes occurred within the upper plane of the subducted Pacific Plate due to downdip compression caused by plate unbending. These earthquakes have a more compact fault area and higher stress drop compared to shallow crustal earthquakes. Additionally, intraslab earthquakes have much slower relative rupture velocity than shallow crustal earthquakes. Good spatial correlations between the static stress drop and slip rate are found, which may suggest the compatibility between dynamic stress drop and static stress drop. The rupture area, average slip, asperity area, average static stress drop over the entire fault, and asperities are consistent with the reported scaling relationship for global intraslab earthquakes within a similar depth range. Using plate unbending, we found the recurrence intervals of these intraslab earthquakes are around 600 years, which is comparable with that of the 2011 Tohoku earthquake. A visual spatial-correlation between the locations of these earthquakes and seismicity in the lower plane is reported. These findings provide insights into the tectonic background and source parameters of intraslab earthquakes in the Tohoku region and contribute to better seismic hazard assessment.

Plain Language Summary

The study analyzes four large intraslab earthquakes that occurred near the Tohoku coast in Japan in the past two decades, with magnitudes of 7.0 or greater. The earthquakes happened within the upper plane of the subducted Pacific Plate due to the plate unbending, which causes compression. The rupture area, average slip, asperity area, and average static stress drop of these earthquakes are consistent with the reported scaling relationship for global intraslab earthquakes. In comparison with shallow crustal earthquakes with similar magnitude, these earthquakes have smaller fault areas, higher stress drop, and slow relative rupture velocity. The recurrence intervals of these earthquakes estimated using the plate unbending mechanism is around 600 years, comparable with the 2011 Tohoku earthquake. The study also reports a spatial correlation between the locations of these earthquakes and seismicity in the lower plane. These findings provide a better understanding of the source parameters of intraslab earthquakes in the Tohoku region and contribute to better seismic hazard assessment.

Introduction

The Pacific Plate (>140 Ma) subducts along the Japan trench at a rate of 88 mm/year (e.g., Kreemer, *et al.,* 2014) under the off-shore region of Honshu Island Japan, creating one of the most seismically active regions in the world and hosting giant megathrust earthquakes, such as the great 2011 Mw 9.1 Tohoku earthquake (e.g., Ide *et al.*, 2011; Shao *et al.*, 2011; Simons *et al.,* 2011). The 2011 Tohoku earthquake nucleated 100 km from the Japan trench axis. Its rupture extended over a broad area with approximate dimensions of 500 km along strike and 200 km along dip (e.g., Ide *et al.*, 2011; Shao *et al.* 2011; Simons *et al.,* 2011). This giant earthquake produced not only a catastrophic seismic hazard but also significantly increased the seismic activity in this region, especially in the vicinity of the area with large coseismic slips (e.g., Toda and Stein, 2022).

Within the enhanced seismological activity following the Tohoku earthquake, three Mw ≥7.0 earthquakes—the 2011 Mw 7.1 Miyagi-Oki earthquake, 2021 M_w 7.1 Fukushima-Oki earthquake, and 2022 Mw 7.3 Fukushima-Oki earthquake (pink stars, Figure 1(a); Table 1)—focussed our attention. These earthquakes occurred at similar centroid depths (~50 km) and had similar thrust focal mechanisms (GCMT, http://www.globalcmt.org). Unlike the 2011 M_w 9 Tohoku earthquake, which ruptured along the plate interface, these three earthquakes occurred within the subducted Pacific Plate. In the Tohoku region of Japan, many researchers have established that intraplate earthquakes define a double-plane seismic zone within the subducted slab over a depth range of 50–200 km (e.g., Umino and Hasegawa, 1975; Hasegawa *et al.,* 1978; Suzuki *et al.,* 1983; Kita *et al.,* 2010; Hasagawa and Nakajima, 2017). The stress regime in the lower plane tends to be a down-dip extension (DDE); whereas in the upper plane, the stress regime tends to be down-dip compression (DDC) (Umino and Hasegawa, 1975; Hasegawa *et al.*, 1978). Kita *et al.* (2010) reported that the thickness of the upper plane is 22 km beneath Honshu island and its nearby region. Based on their locations and focal mechanisms, these three earthquakes result from down-dip compression (DDC) within the upper plane.

Large intraplate earthquakes often have higher seismic hazard impacts than interplate earthquakes within similar magnitude and centroid depth (e.g., Iwata and Asano, 2011). We plot the observed peak ground accelerations (PGAs) at surface K-NET and KiK-net stations (Aoi *et al.,* 2000) from these four intraplate DDC earthquakes in Figures 1(b)-1(e) and compare these observations with those from the 2021/03/20 Mw 7.1 Miyagi-Oki earthquake. The 2021/3/20 Miyagi-Oki earthquake is an interplate thrust earthquake on the plate interface (Figure 1a). This Miyagi-Oki earthquake has a similar centroid depth of 50 km (GCMT, http://www.globalcmt.org) as the 2021/02/13 M_w 7.1 Fukushima-Oki earthquake (e.g., Table 1). As seen in Figures 1(b) -1 (e) the PGAs vary with hypocentral distance (R) as R^{-3} for both intra- and interplate earthquakes when R is less than 200 km. However, for a given distance, the PGAs excited by the intraplate earthquakes are 2.2-4.9 times larger than the interplate earthquake. The difference in PGAs is apparently correlated with the difference in reported damage. The 2021/02/13 M_w 7.1 Fukushima-Oki earthquake produced serious damage to the coastal region of Honshu: two fatalities, at least 186 injuries, and an economic loss of about $1.3 billion (JMA 2021, https://www.bousai.go.jp/updates/r3fukushima_eq_0213/pdf/r3fukushima_eq_higai05.pdf). In contrast, the Mw 7.1 Miyagi-Oki earthquake resulted in 11 minor injuries.

Although the off-shore region of Honshu is seismically very active, Mw 7 or larger intraplate earthquakes are rare. Kita *et al.,* (2010) pointed out that before the 2011 Mw 9 Tohoku earthquake, the 2003 Mw 7.1 Miyagi-Oki earthquake (Figure 1a, Okada *et al.,* 2003) may be the only example of a large intraplate earthquake in 100 years. We notice that the spatial distributions of these large intraplate earthquakes (blue stars, Figure 1a) are not entirely random. In Figure 1a, the dotted orange line denotes the line of the aseismic front, i.e., the downdip limit of interplate earthquakes (Igarashi *et al.,* 2001). The grey circles show the epicenters of relocated lower plate $M_J > 3$ events from 2002 to 2007, which were selected if their locations were >23 km below the plate interface (Kita *et al.,* 2010). The eastern boundary of these earthquakes, marked by a thick black dashed line, is abrupt. We refer to it as the emergence of lower-plane seismicity (**ELPS**). Their focal mechanisms generally reflect the downdip extension (DDE) stress condition in the lower plane (Kita *et al.,* 2010). In map view, the lines of the aseismic front and **ELPS** are close but do not overlap each other. We emphasize that the epicenters of all four Mw ≥7 intraplate earthquakes are within 20 km of **ELPS**. As shown later there is an excellent spatial correlation between **ELPS** and the largest asperities of these earthquakes. In contrast, the epicenter of the 2011/4/11 earthquake is about 40 km east of the line of the aseismic front (Figure 1a). There are notable "gaps" north and south of the 2011/04/07 Miyagi-Oki earthquake. The seismic hazard associated with these possible intraslab DDC earthquakes emphasizes the importance of understanding their causative mechanism and frequency as well as the expected source properties.

In this study, we use strong motion seismic waveforms to study the rupture histories of four intraslab earthquakes that occurred beneath the off-shore region of Honshu. We find that these earthquakes have a higher average stress drop than typical interplate earthquakes, but slower relative rupture velocity. There is a high spatial correlation between the distribution of static stress drop and slip rate. Our 2D strain budget analysis reveals that these earthquakes could have a recurrence interval comparable with that of the great Mw 9 Tohoku earthquake. Because of stress transfer (Lin and Stein, 2004), these earthquakes tend to occur along the down-dip edge of the coseismic rupture of the Tohoku earthquake. We emphasize that special attention should be paid to the "gaps" (Figure 1a) where large magnitude intraslab DDC earthquakes may occur.

Materials and Methods

Using strong motion records of K-NET and KiK-net surface stations (Aoi *et al.,* 2000) along the Tohoku region (Figure 2) we study these four Mw ≥7 DDC intraplate earthquakes. The data were downloaded from the data center of the National Research Institute for Earth Science and Disaster Resilience (NIED). After integrating the acceleration records to velocity, we bandpass filter between 0.05 Hz and 0.3 Hz. We constructed 1D velocity models for the region surrounding the causative fault plane (Table S1-S3), based on a combination of 3D crustal and upper mantle structure (e.g., Matsubara *et al.,* 2019) and the crustal Q model released by the headquarters for earthquake research promotion (e.g., Koketsu *et al.,* 2012). In map view, the source areas of the 2021 and 2022 Fukushima-Oki earthquakes partially overlap (Figure 2); we use the same 1D model for both earthquakes. Because our frequency range is less than 0.3 Hz, for which the influence of a shallow layer is relatively minor, we use the same 1D model for all stations. Theoretical Green's functions are computed using the frequency-wavenumber algorithm of Zhu and Rivera (2002). To correct the timing for 3D wave propagation effects, we select an aftershock (Mw 4-5) near the hypocenter of each mainshock. We compute synthetic waveforms for the aftershock using its network focal mechanism and our assumed 1D velocity structure. At each station, we shift the observed S wave arrival to align with the synthetics. This timeshift is used to align the record of the mainshock at this station.

For each earthquake, we approximate its causative fault as a rectangular fault plane. The strike and dip of this plane are those from the nodal plane of its NIED (F-net) moment tensor solution (Fukuyama *et al.,* 1998) consistent with the aftershock distribution. We adopt the JMA hypocenter for each of the three Tohoku aftershocks. For the 2003 Miyagi-Oki earthquake, we shifted its focal depth from 69 km (JMA) to 62 km so that the initial P and S wave waveforms can be simultaneously fitted. This shift is consistent with the JMA aftershock distribution (Figure 2). The preferred fault plane information is summarized in Table 1.

The fault planes of these earthquakes are discretized into subfaults. We use 4 km × 4 km subfaults for the 2022 event and 2 km × 2 km subfaults for 2003, 2011, and 2021 events. For each subfault, we used the nonlinear finite-fault inversion method of Ji *et al.* (2002) to invert for its slip amplitude, rake angle, rupture initiation time, and rise time which determines the shape of the analytic slip rate function. Details of the method can be found in Ji *et al.* (2002).

Results

We summarize the inversion results for each event. The preferred slip distribution and the cumulative moment-rate function for each event are shown in Figure 3 and Figure 4, respectively. The distributions of the average slip rate, which is defined as the ratio of inverted fault slip and rise time, are shown in Figure 5. The distributions of static stress drop in the direction of fault slip (direction of black arrows in Figure 3), which are estimated using the inverted slip distribution, are shown in Figure 6. The rise-time distributions are shown in Figure S3. The surface projections of the fault slip contours are plotted in Figure 7.

The 2022/03/16 and 2021/02/13 Fukushima-Oki earthquakes

For the 2021 M_W 7.1 Fukushima-Oki earthquake, we adopt a fault plane that orients N28^{o}E and dips 38^o to east-southeast (Table 1) based on its focal mechanism and the distribution of aftershocks in the first month (Figure 2d). A comparison of observations and synthetics for the preferred solution is shown in Figure S5. We find a heterogenous slip distribution that includes several patches with large slip, i.e., asperities (Figure 3b). The largest asperity has a dimension of approximately 20 km along the strike and 10 km downdip, centered about 17 km along the strike and 8 km up-dip (Figure 3b) from the hypocenter. According to JMA, the rupture initiated at a depth of 55.4 km (red star, Figure 3b). About 1 s after the initiation phase (Ellsworth and Beroza, 1995), or perhaps a foreshock, the rupture propagated obliquely back along strike (N208^{o}E) and up-dip toward the largest asperity. The rupture velocity is path dependent; the rupture along the path, highlighted by a black arrow (Figure 3b), has a velocity of about 2 km/s. The failure of the largest asperity occurred approximately 6 s to 13 s after the hypocentral nucleation. This asperity produced the largest pulse in its moment rate function (blue line, Figure 4). We find a seismic moment of 4.9×10^{19} Nm, yielding Mw 7.1. The peak slip is about 3.5 m. Most of the seismic moment was released in the first 14s. We subsequently calculate the distributions of slip rate (ratio of inverted fault slip and rise time at individual subfaults, Figure 5b) and static stress drop (Figure 6b). Both distributions are spatially heterogeneous. The slip rate changes from 0 to 4.4 m/s and static stress drop varies from -12.0 to 46.3 MPa. Because the subfaults with large slip are often better constrained (Ji *et al.*, 2002), we estimate the weighted average slip rate $\bar{\dot{D}}$ and weighted average static stress drop $\Delta\sigma_E$ defined as (Ji *et al.,* 2002),

$$\bar{\dot{D}} = \frac{\sum_1^N D^i (D^i/{T_R}^i)}{\sum_i^N D^i} \qquad (1)$$

$$\Delta\sigma_E = \frac{\sum_1^N D^i \Delta{\sigma_s}^i}{\sum_i^N D^i} \qquad (2)$$

Here *N* denotes the total number of subfaults. For the ith subfault, D^i, ${T_R}^i$and $\Delta{\sigma_s}^i$ represent its slip, rise time, and the static stress drop in the direction of fault slip, respectively. Because $\Delta\sigma_E$ is twice the ratio of apparent "available elastic energy" to the seismic potency (Shao *et al.,* 2012), $\Delta\sigma_E$ is also referred to as the "energy-based static stress drop" (Noda *et al.* 2013). By definition,

$\bar{\dot{D}}$ and $\Delta\sigma_E$ reflect more of the rupture of asperities than a simple average over the entire fault. The near-fault strong ground motion and high-frequency far-field radiation are dominated by the rupture of these asperities (e.g., Somerville *et al.,* 1999; Irikura and Miyake, 2011). For this earthquake, we obtain $\bar{\dot{D}}$ of 1.03 m/s and $\Delta\sigma_E$ of 16.1 MPa (Table 2).

While the rupture velocity is strictly path dependent (Figure 3), we can estimate a slip-weighted average rupture velocity $\overline{V_R}$ as

$$\overline{V_R} = \frac{\sum_1^N D^i L^i / T^i}{\sum_i^N D^i} \qquad (3)$$

where L^i and T^i are the distance from the center of the i^{th} subfault to the hypocenter and the time the center of the i^{th} subfault starts to rupture, respectively. With this definition $\overline{V_R}$ is 1.79 km/s. The significance of $\bar{\dot{D}}$, $\Delta\sigma_E$ and $\overline{V_R}$ are discussed later.

We notice positive spatial correlations between the fault slip (Figure 3b), slip rate (Figure 5b), and static stress drop (Figure 6b). The subfaults with higher slips often have higher slip rates and high static stress drop. In Table 3, we provide the spatial correlations among fault slip, slip rate, and static stress drop defined as:

$$cor_{\Delta\sigma}^{D} = \frac{\sum_1^N D_i \Delta\sigma_i}{\sqrt{\sum_1^N {D_i}^2 \sum_1^N {\Delta\sigma_i}^2}} \qquad (4a)$$

$$cor_{T}^{D} = \frac{\sum_1^N D_i T_i}{\sqrt{\sum_1^N {D_i}^2 \sum_1^N {T_i}^2}} \qquad (4b)$$

$$cor_{\dot{D}}^{D} = \frac{\sum_1^N D_i \dot{D}_i}{\sqrt{\sum_1^N {D_i}^2 \sum_1^N {\dot{D}_i}^2}} \qquad (4c)$$

$$cor_{\Delta\sigma}^{\dot{D}} = \frac{\sum_1^N \dot{D}_i \Delta\sigma_i}{\sqrt{\sum_1^N {\dot{D}_i}^2 \sum_1^N {\Delta\sigma_i}^2}} \qquad (4d)$$

Here D_i, T_i, $\dot{D}_i$, and $\Delta\sigma_i$ are slip, rise time, slip rate (=D_i/T_i), and static stress drop at the ith subfault. All correlations are larger than 0.75 with the correlation between fault slip and slip rate being 0.85 (Table 3).

The 2022 Mw 7.3 Fukushima-Oki earthquake is the largest in this group of intraslab earthquakes. We have slightly adjusted the fault strike inferred from its NIED moment tensor solution (Fukuyama *et al.,* 1998) to match the distribution of the JMA aftershocks during the first month. This results in a fault plane orienting N15^{o}E and dipping 43^o to east-southeast (Figure 2e). Our preferred model explains the observations well (Figure S4). The inversions show that the 2022 Fukushima-Oki mainshock features two major asperities (Figures 2 and 4). The largest asperity has a dimension of 16 km (along strike) and 20 km (downdip), centered about 22 km along strike from the hypocenter (Figures 3a and 6a). A second asperity, centered 5 km back-strike and 8 km downdip from the hypocenter, is not as well constrained. According to JMA, the rupture initiated at 56.6 km depth in the vicinity of the secondary asperity (Figure 6a). After a weak initiation (~2 seconds), the rupture propagated mainly unilaterally in the along-strike direction with a speed of about 2 km/s (black arrow, Figure 3a), leading to the failure of the largest asperity at about 6 s. The rupture front also migrated in the downdip direction but at a much slower velocity (~ 1 km/s), breaking a secondary asperity (Figures 3a and 6a). The seismic moment is 1.05×10^{20} Nm, yielding M_w 7.3. The peak slip is about 3.4 m. Most of the seismic moment occurred in the first 16.5 s (Figure 4). The slip-weighted slip rate ($\bar{\dot{D}}$) is 1.17 m/s, rupture velocity ($\overline{V_R}$) 1.66 km/s, and slip-weighted stress drop $\Delta\sigma_E$ 11.24 MPa. Similar good spatial correlations between the fault slip (Figure 3a), slip rate (Figure 5a), and stress drop (Figure 6a) can be seen. Their spatial correlations are summarized in Table 3.

The JMA epicenter of the 2022 Mw 7.3 Fukushima-Oki earthquake (37.697°N, 141.622°E) is 7.6 km west-southwest (N118°W) of the JMA epicenter of the 2021 Fukushima-Oki earthquake (Figure 1a). These two Fukushima-Oki earthquakes have similar fault strikes (N15°E vs. N28°E) and fault dip (38° vs. 43°). Although in map view the fault planes of these two earthquakes overlap each other (Figure 7), their co-seismic fault planes are separated. The hypocenter of the 2022 Fukushima-Oki earthquake is 4.5 km beneath the fault plane of the 2021 Fukushima-Oki earthquake, suggesting an echelon structure. As shown in Figure 7 the largest asperities of these two earthquakes do not overlap each other. This is important when we try to understand the mechanics of these earthquakes.

The 2011/4/7 Mw 7.1 Miyagi-Oki earthquake

The 2011 Mw 7.1 Miyagi-Oki earthquake occurred less than one month after the 2011 Mw 9 Tohoku earthquake. The focal mechanism and the relocated aftershocks (Nakajima *et al.,* 2011) suggest a fault plane orienting N20°E and dipping 40° to the west—similar to the two Fukushima-Oki earthquakes. Our preferred faulting model produces good agreement between the observations and the synthetics (Figure S6). The faulting model shows that the 2011 Miyagi-Oki earthquake initiated at the downdip edge of its largest asperity (Figure 3c). After a weak initiation (about 1 s), the rupture propagated obliquely along the strike and up-dip directions at a speed of ~2.3 km/s (black arrow, Figure 3c) before breaking the largest asperity. The total seismic moment is 5.0×10^{19} Nm, M_w 7.1. The peak slip is 3.1 m. Most of the seismic moment was released in the first 13 s (Figure 4). As with the other earthquakes that we analyzed we find a strong spatial correlation between the fault slip (Figure 3c), slip rate (Figure 5c), and stress drop (Figure 6c, Table 1). The slip weighted slip rate ($\bar{\dot{D}}$), rupture velocity ($\overline{V_R}$), and $\Delta\sigma_E$ are 1.18 m/s, 1.93 km/s and 14.55 MPa, respectively.

2003/5/26 Mw 7.1 Miyagi-Oki earthquake

The preferred fault plane of the 2003 Mw 7.0 Miyagi-Oki earthquake orients N190^{o}E and dips 69^{o} to the west. A comparison of the observed ground motion and synthetics is shown in Figure S7. The slip distribution is fairly simple (Figure 3d). Most slip occurred on a patch roughly 20 km by 16 km where the peak slip is 2.5 m. The rupture initiated at its southern edge and propagated primarily in the back-strike direction (N20^{o}E) for about 13 km. The rupture speed is slow. Along the direction highlighted by the black arrow (Figure 3d), the rupture speed is about 1.7 km/s. The total seismic moment is 3.4x10^{19} Nm, giving M_w 7.0. Most of the seismic moment was established in the first 10s. The slip weighted slip rate ($\bar{\dot{D}}$), rupture velocity ($\overline{V_R}$), and $\Delta\sigma_E$ are 0.80 m/s, 1.63 km/s and 11.60 MPa, respectively. The correlation between fault slip and slip rate is low (0.7) in comparison with the other three earthquakes (>0.81, Table 3).

Discussion

As shown in Figure 1, the surface projections of the fault planes of three DDC earthquakes since 2011 are near the downdip edge of the co-seismic slip of the 2011 Tohoku earthquake (Shao *et al.,* 2011). The surface projections of these Tohoku DDC aftershocks lie within the 40 km and 50 km iso-depth contours of the subduction interface (Nakajima and Hasegawa, 2017). Although the detailed slip distribution in the downdip direction is limited by the azimuthal coverage of strong motion stations, the centroid depths are well constrained. From north to south, the centroid depths estimated using inverted finite fault slip models decrease slightly from 57 km (the 2011 earthquake), to 55 km (the 2022 earthquake), to 52 km (the 2021 earthquake). Our centroid depths are about 2-4 km shallower than the centroid depths from GCMT solutions (changing from 53.3 km to 50 km, Table 1). Importantly, the centroid depths of these three earthquakes are 5-10 km below the subducted interface. The width of the upper plane of the double seismic zone is ~22 km (Kita *et al.,* 2010). The P axes of the focal mechanisms are sub-horizontal with azimuths of 281°-300°, consistent with the plate convergence direction between Pacific Plate and North America Plate (~295°, GSRM V2.1, Kreemer, *et al.,* 2014).

Such intraplate seismicity within the upper plate of the subducted slab was reported to be strongly affected by the megathrust earthquakes along the plate interface (Astiz *et al.*, 1988; Lay *et al*., 1989). Most large intraslab compressional (DDC) earthquakes in the intermediate depth range occurred following the large (Mw>8.5) interplate rupture (Lay *et al.,* 1989). A similar temporal correlation was also reported between megathrust earthquakes and outer-rise tensional earthquakes (Christenson and Ruff, 1983; Lay *et al.,* 1989). The observed temporal pattern, i.e., infrequent Mw 7 intraslab thrust earthquakes before the 2011 Mw 9 Tohoku earthquake (Kita *et al.*, 2010) and three such earthquakes within the following 11 years, is consistent with this temporal pattern of the global seismicity (Lay *et al.,* 1989). The dip angle of the slab interface is about 18° above the hypocenters of the three Mw >7 Tohoku DDC aftershocks, and ~27° above the hypocenter of the 2003 Miyagi-Oki earthquake (Table 1). Thus, the dip angles (θ) of the fault planes relative to the plate interface vary from 42° to 61°, consistent with the hypothesis that these intraplate DDC earthquakes occurred on pre-existing normal faults of the outer-rise region (e.g., Nakajima *et al.,* 2011; Ranero *et al.,* 2003).

The presence of four Mw 7 and larger DDC intraslab earthquakes within two decades offers a rare opportunity to investigate their shared rupture characteristics. In the following section, we first examine the kinematic and dynamic rupture properties of these intraslab DDC earthquakes. Moreover, motivated by their high seismic hazard potential (as depicted in Figure 1(a)), we also try to investigate their recurrence interval under a framework of plate unbending mechanism.

General characteristics of large DDC intraslab earthquakes

The rupture initiation of these large intraslab DDC earthquakes is similar to shallow crustal earthquakes. Spatially, each rupture is initiated in the vicinity of a large slip patch or asperity (Figure 3, Mai *et al.* 2005). Temporally, each rupture started with a weak initiation phase with a duration of 1-2 s (Ellsworth and Beroza, 1995).

However, the rupture velocity of intraslab DDC earthquakes relative to the S wave speed in the source region (β) is considerably slower than the typical relative rupture velocity of crustal earthquakes (~0.7-0.8β, Kanamori, 1994; Ji and Archuleta, 2021). As shown in Figure 3, the rupture velocity from the hypocenter to the major asperities varies from about 1.0 km/s to 2.3 km/s, less than 51% of β (4.5 km/s, Table S1, S2 S3). The slip-weighted average rupture velocities of these earthquakes ($\overline{V_R}$), which are more sensitive to the rupture time of fault patches with large co-seismic slip, are also slow, varying from 1.6 km/s to 1.9 km/s (0.36-0.43β).

The low relative rupture velocity is consistent with our estimates of seismic radiation efficiency η_R, which is defined as $\eta_R = 2\mu(E_R/M_0)/\Delta\sigma_E$, where E_R is radiated seismic energy and μ is the rigidity in the source region (e.g., Kanamori and Heaton, 2000). We estimate E_R from the moment rate functions of the rupture process determined through the inversion (Vassiliou and Kanamori, 1982). η_R varies from 0.045 to 0.18 with a geometric mean of 0.085. These values are considerably lower than the average of shallow crustal earthquakes (0.25-1.0, Venkataraman and Kanamori, 2004) or Mw>7 megathrust earthquakes (~0.39, Ye *et al.,* 2016) but are consistent with the previous reports of the intermediate depth earthquakes (0.09, Poli and Preto, 2016). Lower η_R indicates that the most of available strain energy was used to break the fault (e.g., Kanamori and Heaton, 2000). From an energy balance consideration near the rupture tip, the relative rupture velocity should be positively correlated with η_R (Andrews, 1976; Kanamori and Rivera, 2006). We then suspect that the observations of both lower relative rupture velocity and lower η_R are the consequences of reactivating pre-existing outer-rise fault planes.

All four earthquakes have spatially heterogeneous slip distributions (Figure 3), which require more than one parameter to depict their general characteristics. We have estimated the rupture area (A), average slip (D), and asperity area (A_a) of each of these earthquakes. Following Somerville *et al.,* (1999), the rupture area (A) is defined as a rectangle consisting of subfaults whose slip is greater than 0.3 times the average slip (D). The asperity area (A_a) is a part of the rupture area consisting of subfaults whose slip is more than 1.5D. The results are summarized in Table 2. Each parameter generally increases with the seismic moment. The scaling relations of A, D, and A_a with seismic moment are crucial for predicting strong ground motion for future earthquakes (e.g., Somerville *et al.,* 1999; Irikura and Miyake, 2011). Arai *et al.* (2015) and Sasatani *et al.* (2006) regressed the self-similar scaling relations of D, A and A_a for large Japanese inrtaslab earthquakes. Iwata and Asano (2011) further expanded such an analysis for large global intraslab earthquakes. They used a dataset including 12 Mw 6.6-8.3 events with focal depths ranging from 35 km to 108 km; however, their dataset includes only one DDC earthquake–the 2003 Mw 7 Miyagi-Okiearthquake. Iwata and Asano (2011) assumed $D \propto {M_0}^{1/3}$, $A \propto {M_0}^{2/3}$, and $A_a \propto {M_0}^{2/3}$; for a given magnitude D, A, and A_a are log-normal distributed. The black solid and dashed lines in Figures 8a-8c show their scaling relations Our estimates of D, A, and A_a for these four DDC earthquakes agree remarkably well with these relations. For a given magnitude, intraslab earthquakes generally have smaller D and A in comparison with shallow crustal earthquakes (Somerville *et al.,* 1999, Iwata and Asano, 2011).

However, for these four earthquakes the geometric mean of A_a/A ratio is 0.216, which is nearly identical to previously reported ratios for shallow crustal earthquakes (~0.22) and interplate thrust earthquakes (~0.25) (Irikura and Miyake, 2011).

Heterogeneous slip distributions lead to heterogeneous static stress drop distributions (Figure 6), which again are difficult to describe with a single parameter. Here we determine and compare three different average static stress drop estimates. First, using seismic moment and fault area A, the average static stress drop over the entire fault $\Delta\sigma_s$ can be estimated with the relation $\Delta\sigma_s \sim 2.44 M_0/A^{3/2}$(Kanamori and Anderson, 1975). Although this formula was derived from a circular crack model (Eshelby, 1957), it is also a fairly precise approximation for rectangular faults if the fault's aspect ratio is less than four (Noda *et al.,* 2013). The $\Delta\sigma_s$ of these four earthquakes changes slightly from 4.6 MPa to 6.3 MPa. Their geometric mean is 5.7 MPa with a factor of 1.16 uncertainty. The average $\Delta\sigma_s$ is slightly larger (24%) than the average $\Delta\sigma_s$of 4.6 MPa reported by Iwata and Asano (2011) for intraslab earthquakes and about 2.5 times of the average stress drop of shallow crustal earthquakes (~2.3 MPa) estimated using the same approach (Somerville *et al.,* 1999). Second, if replacing the seismic moment M_0 and rupture area A with the cumulative asperity seismic moment (${M_0}^a$) and cumulative asperity rupture area (A_a), one can define a stress drop ${\Delta\sigma_s}^A$ using the same formula. This ${\Delta\sigma_s}^A$ can be viewed as a proxy for the average static stress drop over the asperity area (Irikura and Miyake, 2011). For four DDC earthquakes, it changes from 14.3 MPa to 22 MPa with a geometric mean of 17.7 MPa and a factor of 1.2 uncertainty. It is 1.7 times of the mean ${\Delta\sigma_s}^A$ of shallow crustal earthquakes (10.5 MPa, Irikura and Miyake, 2011). We recognize that the rigidity of the source region for these intraslab earthquakes (6.7×10^4 MPa) is about two times larger than shallow inland crustal earthquakes (3.3×10^4 MPa). The roughly a factor of two difference in average $\Delta\sigma_s$ and ${\Delta\sigma_s}^A$

between intraslab and crustal earthquakes can be explained using the hypothesis that the mean strain drop (rather than stress drop) of earthquakes is magnitude independent (e.g., Vallee, 2013). Third, the above two stress drop estimates do not consider the heterogeneous static stress drop distributions (Figure 6) derived from the inverted slip distribution. The slip-weighted average $\Delta\sigma_E$ (equation 2) of an earthquake is estimated using its slip distribution (Figure 3) and static stress drop distribution (Figure 6) and can be viewed as the weighted measure for the static stress drop of the entire rupture. For these four events, $\Delta\sigma_E$ changes from 11.2 MPa to 16.1 MPa with a geometric mean of 13.2 MPa and a factor of 1.2 uncertainty. By definition, $\Delta\sigma_E$ is most sensitive to the fault patches with higher slips. So it is closer to $\Delta{\sigma_s}^A$ than $\Delta\sigma_s$. Note this mean $\Delta\sigma_E$ is about 4 times the mean $\Delta\sigma_E$ of Mw>7 subduction earthquakes (3.44 MPa, Ye *et al.*, 2016). We find that inequality relation $\Delta\sigma_s \leq \Delta\sigma_E \leq \Delta{\sigma_s}^A$ holds for each of these four earthquakes. However, relative to $\Delta\sigma_s$ and $\Delta{\sigma_s}^A$, $\Delta\sigma_E$ is sensitive more to the fine-scale slip/stress drop variations on the fault surface (Noda e*t al.,* 2013; Adams *et al.,* 2019), which is limited by the highest frequency that can be modeled and subfault size. $\Delta\sigma_E$ estimated using finite fault slip models is close to its lower bound (Adams *et al.,* 2019).

We notice good spatial correlations between the distributions of fault slip, slip rate, and static stress drop for a given earthquake (Figures 3, 5, and 6). The correlation between the slip and static stress drop $cor^{D}_{\Delta\sigma}$ changes slightly from 0.81 to 0.90 with a mean of 0.86. The correlation between fault slip and slip rate ($cor^{D}_{\dot{D}}$, 0.81-0.90) is as high as $cor^{D}_{\Delta\sigma}$, though the correlation of the fault slip and rise time varies significantly among the four earthquakes (0.47-0.75). The correlation between static stress drop and slip rate ($cor^{\dot{D}}_{\Delta\sigma}$) varies from 0.69 to 0.78, also significant. While high $cor^{D}_{\Delta\sigma}$ is expected (e.g., Noda, *et al.,* 2013; Adams *et al.,* 2019), the high $cor^{\dot{D}}_{\Delta\sigma}$ is less documented but may shed the light on the relationship between the static stress drop and dynamic stress drop. For the steady state slip pulse model, Kanamori (1994) showed that one can estimate the dynamic stress drop (or effective stress drop in Brune (1970)) as

$$\Delta\sigma_d = \frac{2}{\pi}\mu\langle\hat{V}\rangle/V_R \qquad (5)$$

here $\langle\hat{V}\rangle$ is the average slip velocity on one side of the fault and V_R is the rupture velocity. As shown in Table 2, the slip-weighted average slip rate $\bar{\dot{D}}$ changes from 0.8 m/s to 1.17 m/s. If we assume a log-normal distribution for $\bar{\dot{D}}$, the expected values of $\bar{\dot{D}}$ is 1.03 m/s with a factor 1.2 uncertainty. Approximating $\langle\hat{V}\rangle$ as $\bar{\dot{D}}/2$ and V_R as slip weighted average rupture velocities $\overline{V_R}$, the inferred $\Delta\sigma_d$ from equation (5) changes from 10.4 MPa to 15.0 MPa with a geometric mean of 12.6 MPa. The mean $\Delta\sigma_d$ is in good agreement with the mean slip-weighted average $\Delta\sigma_E$ (13.2 MPa) obtained above. Although there are several assumptions in estimating $\Delta\sigma_d$ and uncertainties, the agreement suggests that $\Delta\sigma_d$ and $\Delta\sigma_E$ are comparable (e.g., Heaton, 1990; Kanamori, 1994;; Ji and Archuleta, 2021).

In short, the rupture characteristics of these intraslab DDC earthquakes are generally consistent in terms of rupture area (A), average slip (D), asperity area (A_a), average static stress drop over entire fault ($\Delta\sigma_s$) and asperities ($\Delta{\sigma_s}^A$). These earthquakes feature more compact fault areas and then higher stress drop in comparison with shallow crustal earthquakes. Intraslab DDC earthquakes also have abnormally slower relative rupture velocity than shallow crustal earthquakes (e.g., Kanamori, 1994; Heaton, 1990). The inferred slip-weighted average dynamic stress drop is comparable with the slip-weighted average static stress drop.

Temporal correlation, Strain budget, and seismic hazard

The intraplate DDC earthquakes in the Japan subduction zone have been interpreted as the result of plate unbending (e.g., Kawakatsu, 1986; Wang, 2002; Sandiford *et al.*, 2020).

Kawakatsu (1986) showed numerically that the strain rate due to the plate unbending is large enough to account for the seismic strain rate observed at several subduction zones, including Tohoku, in a depth range from 50 km to 200 km. The largest intraslab earthquake near Tohoku that Kawakatsu (1986) predicted has an m_b of 6.5, which is equivalent to an Mw of 7 using the relation Kawakatsu (1986) adopted. The significant seismic hazard caused by the four Mw 7 and larger intraslab DDC earthquakes and their distribution along the subduction zone (e.g., Figure 1(a) and Figure 7) draw our attention to the areas between these earthquakes, namely, the area between the 2022 Fukushima-Oki earthquakes and the 2011 Miyagi-Oki earthquake, and the region between the 2003 and 2011 Miyagi-Oki earthquakes. Along the coast parallel direction, the lengths of these regions are comparable with that of the 2021 M_w 7.1 Fukushima-Oki earthquake (Figure 7). In principle, the subducted slab beneath these regions can host similar Mw 7 intraplate DDC earthquakes. However, the temporal correlation between the megathrust and large intraslab DDC earthquakes (Lay *et al.,* 1989) suggests that these regions might have already experienced similar Mw ~7 DDC earthquakes following the previous Tohoku type earthquake. From a perspective of seismic hazard evaluation, it is important to know whether the unbending strain/stress loading during the inter-seismic period before the 2011 M 9 Tohoku earthquake is sufficient to produce another intra-slab Mw 7 DDC earthquake at the same place.

The recurrence interval of the 2011 Tohoku earthquake has been extensively studied as a parameter in assessing seismic hazards. Nakata *et al.* (2016) reviewed geological data of tsunami sediments, historical documents, and previous 2D numerical modeling results, which suggest that the recurrence interval of the Mw 9 earthquakes in the Tohoku-Oki region ranges from 500 to 1000 yrs. Based on their comprehensive 3D simulations, Nakata *et al.*, (2016) obtained a recurrence interval of 700-770 years (Nakata *et al.*, 2016). Therefore, it is reasonable to use 750 years as a proxy for its recurrence interval.

To estimate the unbending strain rate within the upper plane, we consider a simple 2D subduction flexure model along the plate motion direction, as shown in Figure 9. Under the outer-rise region in front of the Japan trench, the Pacific Plate bends, resulting in an extensional upper plane (blue region), compressional lower plane (red region), and a neutral plane in between (Figure 9). Such stress loading results in not only the increasing curvature of the Pacific Plate when it moves toward the trench but also the extensive outer-rise seismicity. Sandiford*, et al.* (2020) recently analyzed the flexure of subducted slabs around the Pacific Ocean using the Slab 1 global slab interface model (Hayes *et al.,* 2012). Their results showed that the maximum curvature (K_{max}) of ~2×10^{-6}/m is acquired at 50 km relative to the trench axis, along the direction of subduction (Figure 9). Plate unbending occurs immediately after the point of the maximum curvature, leading to the change of the stress field within the subducted slab, i.e., compressional upper plane (pink region), extensional lower plane (blue region), and a neutral plane at about 22 km below the plate interface (Kita *et al.,* 2010). Ignoring the temporal variation of slab curvature, the compressional strain rate ($\dot{\varepsilon}_{ss}$)*,* within the upper slab due to plate unbending can be approximated as (e.g., Sandiford*, et al.,* 2020))

$$\dot{\varepsilon}_{ss} \approx y \cdot u_s \frac{\partial K}{\partial s} \qquad (6)$$

K represents the plate curvature; and in this 2D simplification, K is a function of the distance (s) relative to the trench axis along the slab midplane. y denotes the normal distance to the neutral plane; it varies from zero to the thickness of the upper plane (y_{max}). y_{max} was found to be 22 km (Kita *et al.,* 2010). u_s of 88 mm/yr is the plate convergence speed (Kreemer, *et al.* , 2014). While the estimate of $\dot{\varepsilon}_{ss}$ is subject to relatively large uncertainty due to the difficulty in measuring precisely the slab dip angle (Kawakatsu, 1986), we focus our attention on the total upper-plate shortening rate $\dot{\delta}_{total}$ defined as

$$\dot{\delta}_{total} = \int_{s_0}^{s_1} \dot{\varepsilon}_{ss} ds \sim y \cdot u_s (K_{max} - K_{s_1}) \qquad (7)$$

where s_0 denotes the location of the midplane relative to the trench axis where the Pacific Plate has the largest curvature K_{max}. In Standiford *et al.* (2020), s_0 was found to be ~50 km and K_{max} is 2×10^{-6}/m. When s_1 is large, for example s_1 =400 km, the depth of the slab interface is about 150 km and K_{s_1} can be ignored. $\dot{\delta}_{total}$ then changes from 0 to 3.9 $\times10^{-3}$m/yr, with a mean $\overline{\dot{\delta}_{total}}$ of 1.9×10^{-3}m/yr in the slab normal direction.

For the large DDC earthquakes that break through the majority of the upper plane, the average along slab shortening released by a thrust earthquake can be approximated as $D\cos\theta$: D and θ are average fault slip and the dip angle relative to slab interface, respectively (e.g., Kawakatsu, 1986). As shown in Table 1, the average fault slip *D* varies from 0.76 m to 1.6 m. We determined the dip angle of the slab interface, which is about 18^{o} above the hypocenters of the three Tohoku aftershocks, and ~27^{o} above the hypocenter of the 2003 Miyagi-Oki earthquake (Table 1). The along-slab shortening caused by these earthquakes varies from 0.43 m to 0.76 m. If these earthquakes are the response to the total upper plate shortening, their mean recurrence intervals would be about 301 yrs (225 yrs to 394 yrs using the values of individual earthquakes). However, small intraplate DDC earthquakes also contribute to the total unbending strain budget of the upper plate. Let us assume that the DDC earthquakes within the upper plane obey the Gutenberg and Richter relation, $log10(N) = a - bM_w$, N denotes the number of earthquakes with moment magnitude M_w or larger (Gutenberg and Richter, 1956) and b is 1. These M_W 7 DDC earthquakes broke through the majority portion of the upper plane, it is reasonable to treat them as the maximum magnitude intraslab DDC earthquakes (Kawakatsu, 1986). The ratio between the total seismic moment of small magnitude intraplate DDC earthquakes and these M_W 7 earthquakes is 1 (e.g., McGarr, 2014). If cumulatively these small DDC earthquakes make a similar contribution to the plate shortening as M_W 7 earthquakes, the average recurrence interval of M_W 7 earthquakes will be a factor 2 larger, i.e., 600 yrs (450 yrs to 788 yrs).

This strain budget analysis suggests that the upper plane of the subducted slab is in a relatively high-stress stage but cannot predict the exact locations of large DDC earthquakes. Lin and Stein (2004) pointed out that the static Coulomb stress perturbation created by the megathrust, such as the 2011 Tohoku earthquake, will promote thrust faulting within the subducted slab near the downdip edge of the mainshock rupture if it is close to failure. The locations of three DDC earthquakes since 2011 are consistent with this interpretation (Figure 1(a)). The spatial correlation between these earthquakes and the aseismic deformation front (Figure 1(a)) might reflect the fact that giant earthquakes rupture nearly the entire locked interface. However, the exception, i.e., the 2003 Miyagi-Oki earthquake, does exist.

Furthermore, in this study, we also observe a visual correlation between the line of the emergence of lower-plane seismicity (**ELPS**, Figure 9) and the map view of these DDC earthquakes (Figure 1(a) and Figure 8). We suspect that such a correlation is not coincidental. The relocated lower-plane seismicity occurred between 2002 and 2007 (Kita *et al.,* 2010). Even before the great Tohoku earthquake, the extension stress of the lower plane reached the brittle failure stage. Stevens and Avouac (2021) recently reported that the seismicity rate is proportional to the strain rate measured by geodetic methods. Therefore, the **ELPS** can be interpreted as an indicator of a higher lower-plane strain rate. If the intraslab seismicity in this depth range is mainly a result of plate unbending, the higher lower-plane strain rate must be accompanied by the higher strain rate within the upper plane of subducted slab, right above. We suspect that this is the reason for the visual correlation between **ELPS** and the map view of these DDC earthquakes. The mechanical cause of such strain rate concentration may be attributed to the slab structure. Previous tomographic studies have reported a spatial correlation between the fault planes of the intraslab DDC earthquakes and the heterogeneities within the slab in terms of P and S wave velocity speeds and Poisson's ratio (Mishra and Zhao, 2004; Nakajima *et al.,* 2011; Wang *et al.*, 2022).

We admit that the 2D approximation suffers some uncertainties. Besides average fault slip, the width of the upper plate, K_{max}, and K_{400} etc, the compressional unbending strain may also be released aseismically. Wang (2002) and Kita *et al.* (2006) pointed out that at depth of ~75 km or more, the density increase caused by metamorphic eclogite formation induces a stretching deformation within the subducted oceanic crust. This effect can be large enough to offset the compressional unbending strain and lead to the observation of small normal faulting earthquakes directly beneath the subducted plate interface. Given the short history of modern seismic observations, it is also possible that the large DDC earthquakes that occurred between two megathrusts had already released the cumulative compressional strain, i.e., the 2003 Mw 7.0 Miyagi-Oki earthquake. Nevertheless, the above analyses support our hypothesis that the "gaps" among the four DDC earthquakes along the **ELPS** have high seismic hazard potential. The strain accumulation due to plate unbending during the inter-seismic period (~750 yr) of Mw 9 earthquakes is sufficient to have the repeating occurrence of such M_w 7 intraslab DDC earthquakes. Given the large seismic hazard potential of such intraslab earthquakes, special attention should be made.

Conclusions

Using the finite-fault inversion method we have determined the faulting kinematics of four Mw≥7 compressional intraslab earthquakes that occurred along the Tohoku region in the last two decades. From our analysis, these earthquakes are characterized by slow rupture velocity, high static stress drop, and high spatial correlation between slip rate and static stress drop. Because the source areas for these intraslab events are close to the coast of the Tohoku region, these high-stress drop earthquakes produce higher ground motion than the interplate earthquakes with similar magnitude in the Tohoku region. Understanding the causative mechanism for such intraslab earthquakes is then important for considering potential hazard in this region.

All DDC earthquakes ruptured within the upper plane of the subducted Pacific Plate (Kita *et al.,* 2010), consistent with plate unbending mechanics (Kawakatsu, 1986). We show that the compressional strain loading due to this mechanism is sufficient to support the recurrence of such events in a period of about 600 yrs, comparable with the reported recurrence interval of the 2011 Tohoku earthquake. While plate unbending mechanics cannot precisely predict the event locations, we notice that all four events occurred in the vicinity of the emergence of lower plane seismicity (ELPS), which can be used as a proxy to predict the future locations of such earthquakes. This correlation is consistent with plate unbending mechanics. Alternatively, the occurrence of the three DDC earthquakes since 2011 can also be interpreted as the result of static stress perturbation excited by the 2011 M 9 Tohoku earthquake. We emphasize that special consideration should be given for the area between the 2022 Fukushima-Oki earthquakes and the 2011 Miyagi-Oki earthquake, and the region between the 2003 and 2011 Miyagi-Oki earthquakes, which can host compressional intraslab earthquakes with similar magnitude.

Acknowledgments

We thank Prof. J. Nakajima of the Tokyo Institute of Technology and Dr. S. Kita of the Building Research Institute for relocated seismicity catalogs. Discussions with Drs. Ogawa and Dr. K. Miyakoshi of ORI were critical in improving the content of this study.

Open Research

All strong motion data managed by the National Research Institute for Earth Science and Disaster Resilience can be downloaded freely at the Strong-Motion Seismograph Networks (K-NET and KiK-net) https://www.kyoshin.bosai.go.jp/. Statistical analyses were conducted using MATLAB (R2019b), and figures were generated using Generic Mapping Tools (GMT 6; Wessel et al., 2013).

References

Andrews, D. J. (1976). Rupture velocity of plane strain shear cracks. *Journal of Geophysical Research*, 81(32), 5679–5687.

Adams, M., Hao, J., and C. Ji. (2019), Energy-based average stress drop and its uncertainty during the 2015 Mw 7.8 Nepal earthquake constrained by geodetic data and its implications to earthquake, *Geophysical Journal International*, 217 (2), 784-797.

Aoi, S., K. Obara, S. Hori, K. Kasahara, and Y, Okada. (2000), New strong-motion observation network: KiK-net, *Eos Trans. AGU*, 81(48), Fall Meet. Suppl., Abstract S71A-05.

Arai, K., Dan, K., Ishii, T., Hanamura, M., Fujiwara, H., and Morikawa, N. (2015), Procedure of Evaluating Fault Parameters of Intra-slab Earthquakes for Strong Motion Prediction, *Journal* *of Struct. Construct. Eng. (Transactions of AIJ)*, No. 716, 1537-1547 (in Japanese with English Abstract).

Astiz, L., T. Lay, and H. Kanamori(1988), Large intermediate-depth earthquakes and the subduction process, *Physics of the Earth and Planetary Interiors* 53 (1-2), 80-166

Brune, J. N. (1970), Tectonic stress and the spectra of seismic shear waves from earthquakes, *Journal of. Geophys. Research.*, 75(26), 4997– 5009.

Christensen., D. H., and L, J., Ruff. (1983), Outer-rise earthquakes and seismic coupling, *Geophysical Research Letters*, 10(8):697-700. doi: 10.1029/GL010I008P00697

Courboulex., F., Vallée, M., Causse, M., and Chounet, A. (2016), Stress-Drop Variability of Shallow Earthquakes Extracted from a Global Database of Source Time Functions. *Seismological Research Letters* 2016;; 87 (4): 912–918.

Craig, T. J., A. Copley, and J. Jackson. (2014), A reassessment of outer-rise seismicity and its implications for the mechanics of oceanic lithosphere, *Geophysical Journal International*, **197**, Issue 1,63–89, https://doi.org/10.1093/gji/ggu013

Ellsworth, W. L., and Beroza, G. C. (1995), Seismic evidence for an earthquake nucleation phase, *Science*, 268 (5212): 851-855

Eshelby, J.D. (1957) The Determination of the Elastic Field of an Ellipsoidal Inclusion, and Related Problems. *Proceedings of the Royal Society of London. Series A*, 241, 376-396.

Fukuyama, E., M. Ishida, D. S. Dreger, H. Kawai. (1998), Automated seismic moment tensor determination by using online broadband seismic waveforms, *Zishin* (J. Seismol. Soc. Japan) Ser. 2, **51**, 149-156 (in Japanese with English abstract).

Gutenberg, B. and Richter, C.F. (1956) Earthquake Magnitude, Intensity, Energy and Acceleration. *Bulletin of the Seismological Society of America*, 46, 105-146.

Hasegawa, A., and J. Nakajima. (2017), Seismic imaging of slab metamorphism and genesis of intermediate-depth intraslab earthquakes, *Progress in Earth and Planetary Science*, DOI: 10.1186/s40645-017-0126-9.

Hasegawa, A., N. Umino and A. Takagi, (1978), Double-planed structure of the deep seismic zone in the northeastern, Japan arc, *Tectonophysics*, 47, 43-58.

Hayes, G. P., D. J. Wald, and R. L. Johnson (2012), Slab1.0: A three-dimensional model of global subduction zonegeometries,*Journal of Geophysical. Research.,*117, B01302, doi:10.1029/2011JB00.

Heaton. T.H. (1990), Evidence for and implications of self-healing pulses of slip in earthquake rupture, *Physics of the Earth and Planetary Interiors*,Vol 64. 1-20.

Ide, S., Baltay, A. and Beroza, G. C. (2011), Shallow dynamic overshoot and energetic deep rupture in the 2011Mw 9.0 Tohoku-Oki earthquake. *Science* 332, 1426–1429.

Igarashi, T., T. Matsuzawa, N. Umino , and A. Hasegawa. (2001), Spatial distribution of focal mechanisms for interplate and intraplate earthquakes associated with the subducting Pacific plate beneath the northeastern Japan arc: A triple-plated deep seismic zone, *Journal of Geophysical Research.*, 106, 2177-2191.

Irikura, K., and H. Miyake. (2011), Recipe for predicting strong ground motion from crustal earthquake scenarios, *Pure and Applied Geophysics.*, 168, 85-104, doi:10.1007/s00024-010-0150-9.

Iwata, T. and K. Asano (2011), Characterization of the Heterogeneous Source Model of Intraslab Earthquakes Toward Strong Ground Motion Prediction, *Pure and Applied Geophysics,* 168, 117-124, doi:10.1007/s00024-010-0128-7

Japanese Meteorological Agency. (2021), The report for the 2021 Off-Fukushima earthquake" https://www.jma.go.jp/jma/press/2102/22a/kaisetsu202102221100.pdf. (in Japanese)

Ji, C., and Archuleta, R. J. (2021), Two empirical double-corner-frequency source spectra and their physical implications. *Bulletin of the Seismological Society of America,* 111(2), 737-761.

Ji, C., Wald, D. J., and Helmberger, D. V. (2002), Source description of the 1999 Hector Mine, California, earthquake, part I: Wavelet domain inversion theory and resolution analysis, *Bulletin of the Seismological Society of America,* **92(4)**, 1192-1207.

Kanamori, H. (1994), Mechanics of earthquakes, *Annual Review of Earth and Planetary Sciences* 22 (1), 207-237.

Kanamori, H., and Rivera, L. (2006), Energy partitioning during an earthquake, In: *Earthquakes: Radiated Energy and the Physics of Faulting. Geophysical Monograph Series*. No.170. American Geophysical Union , Washington, DC, pp. 3-13.

Kanamori, H., and Heaton, T.H. (2000), Microscopic and macroscopic physics of earthquakes, *Geocomplexity and the Physics of Earthquakes* 120, 147-163

Kanamori, H., and Anderson, D.L. (1975), Theoretical basis of some empirical relations in seismology, *Bulletin of the Seismological Society of America*, 65 (5): 1073–1095

Kawakatsu, H., (1986), Double Seismic Zones: Kinematics, *Journal of Geophysical Research,* **91**, NO. B5, 4811-4825.

Kita, S., T. Okada, A. Hasegawa, J. Nakajima, and T. Matsuzawa. (2010), Existence of interplane earthquakes and neutral stress boundary between the upper and lower planes of the double seismic zone beneath Tohoku and Hokkaido, northeastern Japan, *Tectonophysics*, doi:10.1016/j.tecto.2010.10.010.

Koketsu, K., H. Miyake, Afnimar and Y. Tanaka. (2012), A proposal for a standard procedure of modeling 3-D velocity structures and its application to the Tokyo metropolitan area, Japan, *Tectonophysics*, **472**, 290-300.

Kreemer, C., G. Blewitt, and E. C. Klein (2014), A geodetic plate motion and Global Strain Rate Model, *Geochem. Geophys. Geosyst.,* 15, 3849–3889, doi:10.1002/2014GC005407.

Lay, T., L. Astiz, H. Kanamori, and D. H. Christensen. (1989), Temporal Variation of Large Intraplate Earthquakes in Coupled Subduction Zones, *Physics of the Earth and Planetary Interiors,* 54, no. 3-4, 258-312. doi:Doi 10.1016/0031-9201(89)90247-1.

Lin, J., and R. S. Stein (2004), Stress triggering in thrust and subduction earthquakes and stress interaction between the southern San Andreas and nearby thrust and strike-slip faults, *Journal of Geophysical Research*, 109, B02303, doi:10.1029/2003JB002607.

Matsubara, M., H. Sato, K. Uehira, M. Mochizuki, T. Kanazawa, N. Takahashi, K. Suzuki and S. Kamiya. (2019), Seismic velocity structure in and around the Japanese Island src derived from seismic tomography including NIED MOWLAS Hi-net and S-net data, *Seismic Waves - Probing Earth System, IntechOpen*, 1-19, doi:10.5772/intechopen.86936.

McGarr, A. (2014), Maximum magnitude earthquakes induced by fluid injection, *Journal of Geophysical Research*, 119, 1008– 1019

Mai, P. M., Spudich, P., and Boatwright, J. (2005), Hypocenter locations in finite-source rupture models. *Bulletin of the Seismological Society of America*, 95(3), 965-980.

Mishra, O. P., and Zhao, D. (2004), Seismic evidence for dehydration embrittlement of the subducting Pacific slab, *Geophysical Research Letters*, 31, L09610.

Nakajima, J., A. Hasegawa, and S. Kita. (2011), Seismic evidence for reactivation of a buried hydrated fault in the Pacific slab by the 2011 M9.0 Tohoku earthquake, *Geophysical Research Letters*, 38, L00G06, doi:10.1029/2011GL048432

Nakajima, J., and A. Hasegawa. (2006), Anomalous low-velocity zone and linear alignment of seismicity along it in the subducted Pacific slab beneath Kanto, Japan: Reactivation of subducted fracture zone?, *Geophysical Research Letters*, 33, L16309, doi: 10.1029/2006GL026773.

Nakata, R., Hori, T., Hyodo, M. *et al.* (2016), Possible scenarios for occurrence of M～7 interplate earthquakes prior to and following the 2011 Tohoku-Oki earthquake based on numerical simulation. *Scientific Reports* 6, 25704.

Noda, H., N. Lapusta, and, H. Kanamori. (2013), Comparison of average stress drop measures for ruptures with heterogeneous stress change and implications for earthquake physics, *Geophysical Journal International* 193 (3), 1691-1712.

Okada, T., N. Umino, and A. Hasegawa. (2003), Rupture process of the July 26 2003 northern Miyagi earthquake sequence, NE Japan, estimated from double-difference hypocenter locations, *Earth Planets, and Space*, 55, 741-750.

Poli, P., and G. A. Prieto (2016), Global rupture parameters for deep and intermediate-depth earthquakes, *Journmal of Geophysical Research*, 121, 8871–8887, doi:10.1002/2016JB013521

Ranero, C., Phipps Morgan, J., McIntosh, K. *et al*. (2003), Bending-related faulting and mantle serpentinization at the Middle America trench. *Nature* 425, 367–373. https://doi.org/10.1038/nature01961

Sandiford, D., L. M. Moresi, M. Sandiford, R. Farrington, and T. Yang. (2020), The Fingerprints of Flexure in Slab Seismicity, *Tectonics*, 39, no. 8. doi: 10.1029/2019TC005894.

Sasatani, T., Morikawa, N., and Maeda, T. (2006), Source Characteristics of Intraslab Earthquakes, *GeophysicaI BuIletin of Hokkaido University*, Sapporo, Japan, No. 69, M arch 2006, pp . 123 -134. (in Japanese with English abstract)

Shao, G. F., and C. Ji. (2012), What the exercise of the SPICE source inversion validation BlindTest 1 did not tell you, *Geophysical Journal International,* **189,** no. 1, 569-590.

Shao, G., Li, X., Ji, C. *et al.* (2011), Focal mechanism and slip history of the 2011 Mw 9.1 off the Pacific coast of Tohoku Earthquake, constrained with teleseismic body and surface waves. *Earth Planets, and Space* 63, 559–564. https://doi.org/10.5047/eps.2011.06.028

Si, H., and Midorikawa, S. (1999), Attenuation Relations for Peak Ground Acceleration and Velocity Considering Effects of Fault Type and Site Condition, *Journal of Struct. Construct. Eng. (Transactions of AIJ)*, No. 523, 63-70 (in Japanese with English Abstract).

Simons, M, *et al.* (2011), The 2011 magnitude 9.0 Tohoku-Oki earthquake: Mosaicking the megathrust from seconds to centuries. *Science* 332.6036: 1421-1425.

Somerville, P. G., K. Irikura, R. Graves, S. Sawada, D. Wald, N. Abrahamson, Y. Iwasaki, T. Kagawa, N. Smith, and A. Kowada. (1999), Characterizing crustal earthquake slip models for the prediction of strong ground motion, *Seismological Research Letters*, 70, 59-80.

Stevens, V. L., and J-P Avouac. (2021), On the relationship between strain rate and seismicity in the India–Asia collision zone: implications for probabilistic seismic hazard, *Geophysical Journal International*, Volume 226, Issue 1, 220–245.

Suzuki, S., Sasatani. T., and Motoya. Y. (1983), Double seismic zone beneath the middle of Hokkaido, Japan, in the southwestern side of the Kurile Arc, *Tectonophysics*, Volume 96, Issues 1–2, 59-76.

Toda, S., and Stein, R.S. (2022), Central shutdown and surrounding activation of aftershocks from megathrust earthquake stress transfer. *Nature Geoscience* 15, 494–500. https://doi.org/10.1038/s41561-022-00954-x

Umino, N., and Hasegawa, A. (1975), On the two-layered structure of deep seismic plane in North-Eastern Japan Arc, *Zishin,* 2nd issue, v27, 125-139. (in Japanese with English Abstract)

Vallée, M. (2013), Source time function properties indicate a strain drop independent of earthquake depth and magnitude. *Nature Communications,* 4, 2606. https://doi.org/10.1038/ncomms3606

Vassliou, M.S., and Kanamori, H.(1982), The energy release in earthquakes, *Bulletin of the Seismological Society of America*, 72 (2), 371-387

Venkataraman, A., and H. Kanamori (2004), Observational constraints on the fracture energy of subduction zone earthquakes, *Journal of Geophysical Research*, 109, B05302, doi:10.1029/2003JB002549.

Wang, K., (2002) Unbending combined with dehydration embrittlement as a cause for double and triple seismic zones, *Geophysical Research Letters,* **29(18),** 1889, doi:10.1029/2002GL015441

Ye, L., T. Lay, H. Kanamori., and L. Rivera. (2016), Rupture characteristics of major and great (Mw ≥ 7.0) megathrust earthquakes from 1990 to 2015: 1. Source parameter scaling relationships, *Journal of Geophysical Research,* 121 (2), 826-844

Zhu, L., and Rivera, L. A. (2002), A note on the dynamic and static displacements from a point source in multilayered media, *Geophysical Journal International,* **148(3),** 619-627

Figure 1

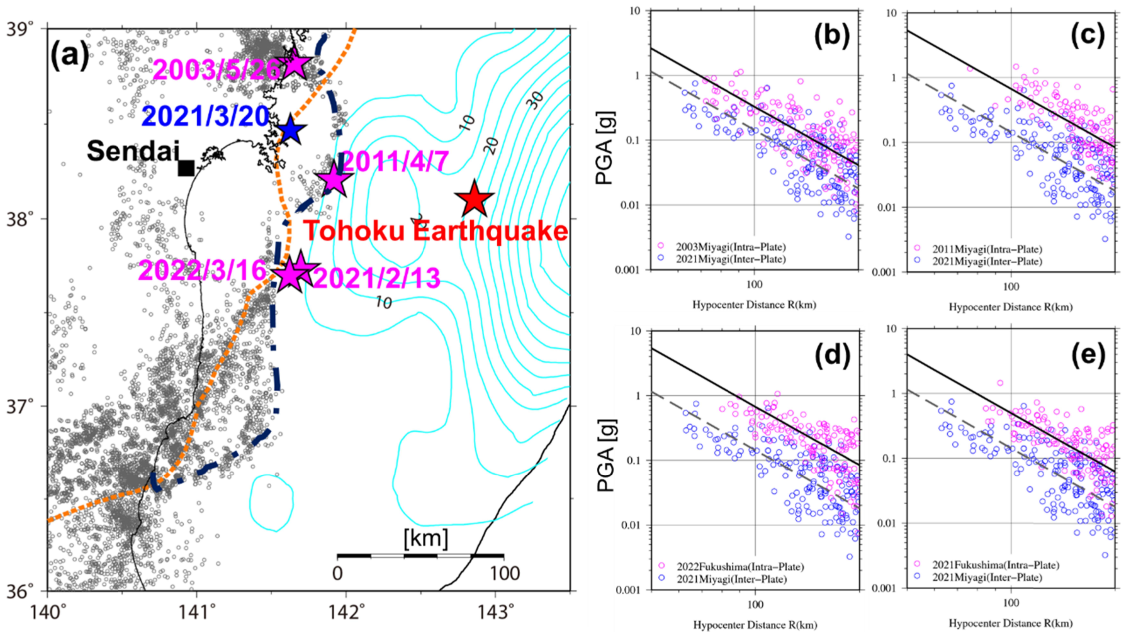

Figure 1 (a) Epicenter locations of four Mw≥7 intraslab earthquakes (pink stars) and the 2021/3/20 Mw 7.1 Miyagi-Oki interplate earthquake (blue star). Grey dots show the relocated seismicity (2002 to 2007) with depths below the neutral zone of the subducted Pacific Plate (Kita *et al.,* 2010). Cyan contours show the slip distribution for the 2011 Tohoku earthquake by Shao *et al.,* (2011). The dotted orange line shows the aseismic line proposed by Igarashi *et al.* (2001). (b)-(f) observed PGAs for the four intraslab earthquakes as a function of hypocentral distances are compared with the observed PGAs for 2021/03/20 Mw 7.0 Miyagi-Oki interplate earthquake (Table S1). The comparisons of observed PGAs with the ground motion prediction equation (Shi and Midorikawa, 1999) for these events are shown in Figure S1.

Figure 2

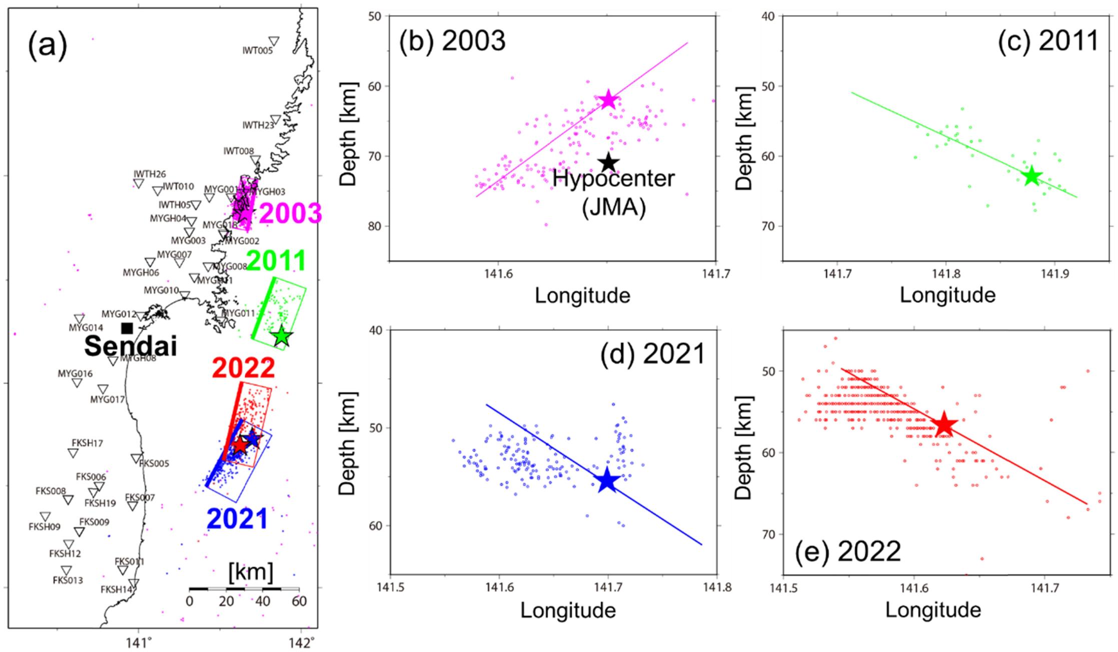

Figure 2 Station distribution and fault geometry for intraplate earthquakes. (a) Distribution of K-NET and KiK-net strong motion stations (triangles) and the surface projections of the fault planes for the four Mw ≥7 intraplate earthquakes analyzed in this study. The colored dots indicate the epicenters of M>3 aftershocks that occurred within one month after the corresponding mainshocks. (b) A vertical cross-section along the strike-normal direction. The solid line is the projection of preferred fault plane for the 2003 Mw 7 Miyagi-Oki earthquake. The dots show the projections of M>3 aftershocks reported by JMA. The black star denotes the JMA hypocenter and the pink star is the hypocenter used in this study.(c) Similar to (b), this section is for the 2011 Mw 7.1 Miyagi-Oki earthquake, which the dots showing the M>3 earthquakes relocted by Nakajima et al. (2011). (d) and (e) are similar to (b) but for the 2021 Mw 7.1 and 2022 Mw7.3 Fukushima-Oki earthquakes, respectively.

Figure 3

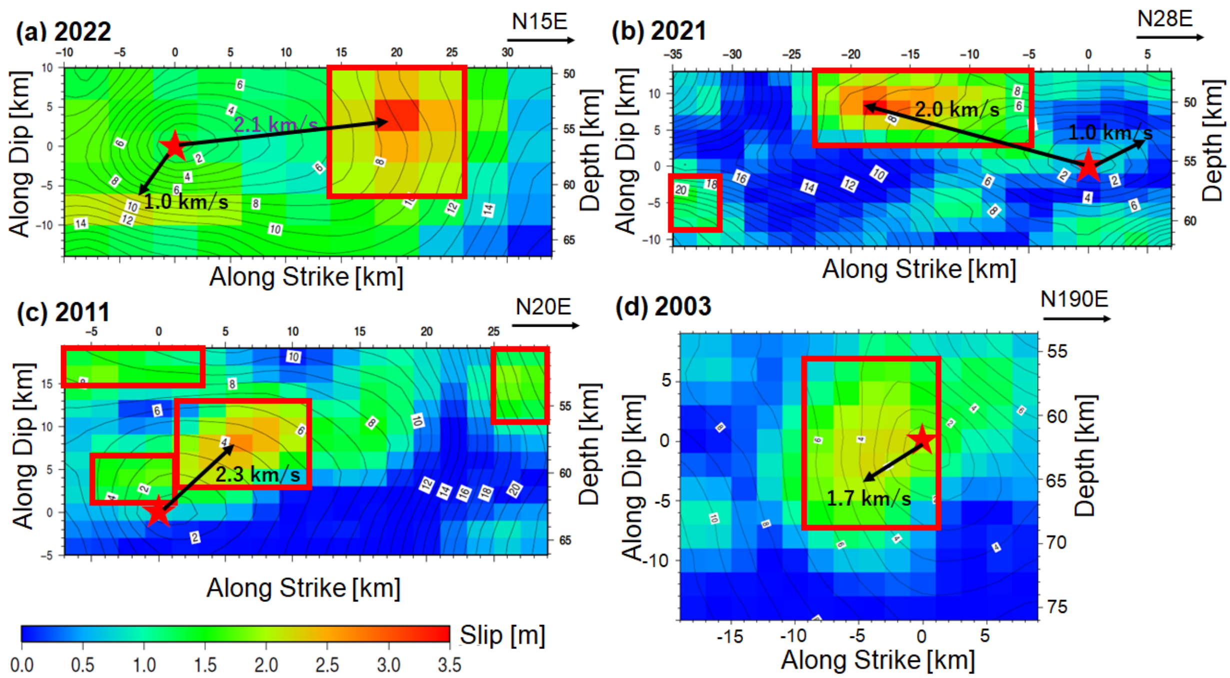

Figure 3. Inverted slip distribution for each earthquake with asperities outlined by red rectangles. For each earthquake the black arrows indicate the rupture propagation direction from the hypocenter (red star) along which the rupture velocity is measured.

Figure 4

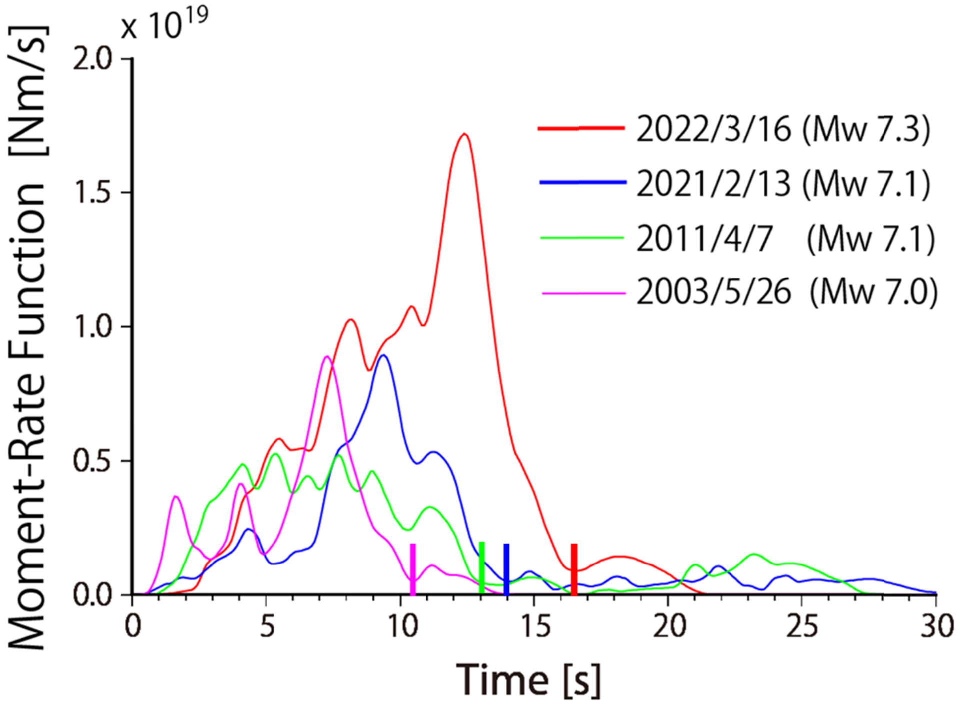

Figure 4: Moment-rate function calculated for each earthquake. The colored vertical bars on the abscissa give the preferred duration estimate for each event.

Figure 5

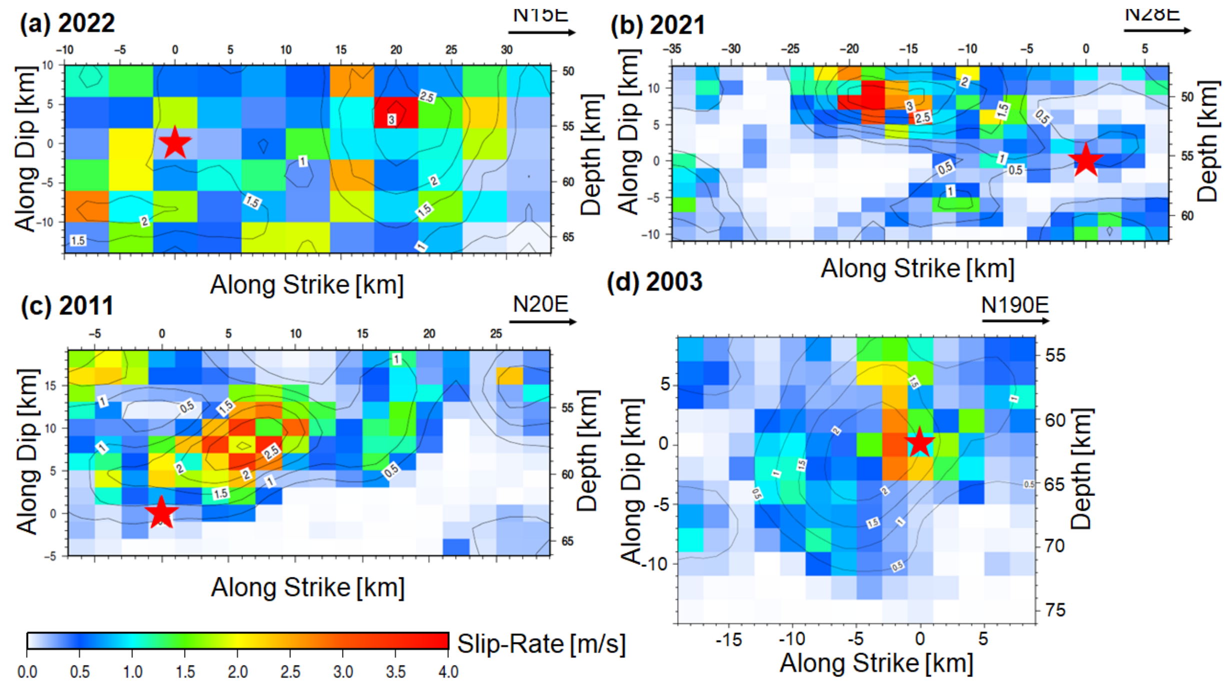

Figure 5: Spatial distribution of slip rate on the fault for each of four DDC earthquakes. The earthquake is labeled by the year in which it occurred . The slip rate is defined as ratio of inverted coseismic slip and rise time. Black lines are contours of the inverted slip. Red stars mark the hypocenters.

Figure 6

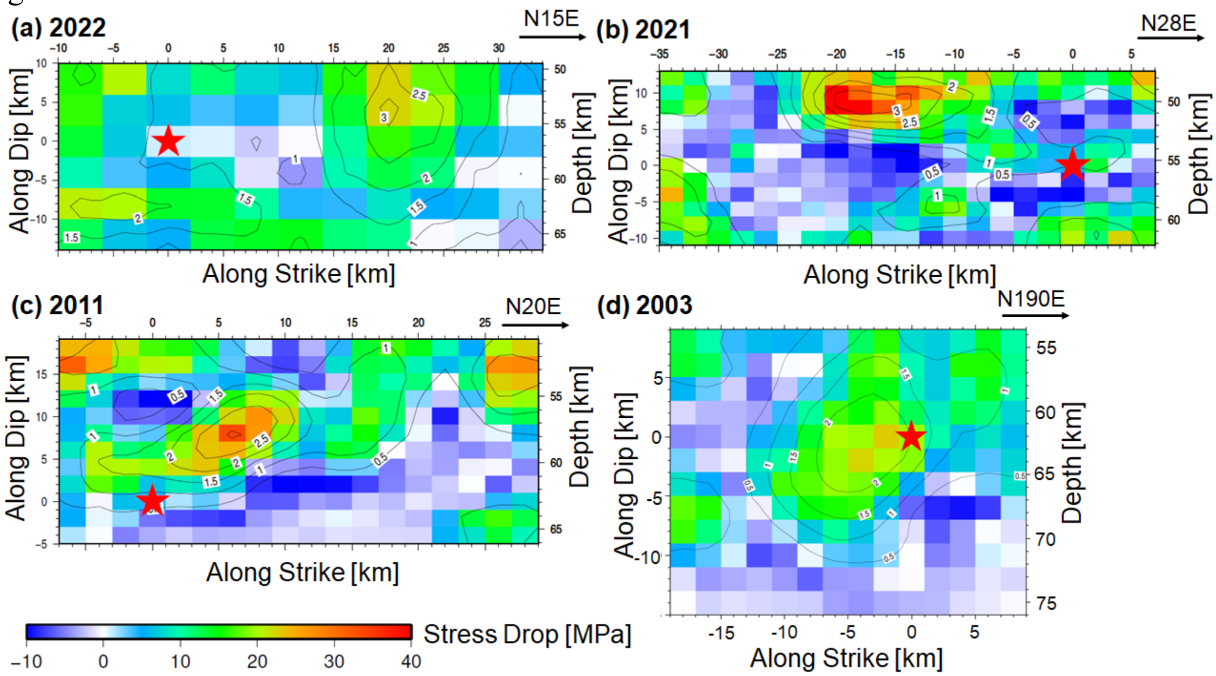

Figure 6: Distribution of static stress drop at the co-seismic slip direction for each of four DDC earthquakes. The earthquake is labeled by the year in which it occurred. Black contours for each map denote the inverted co-seismic slip (Figure 3). Red stars mark the hypocenters.

Figure 7

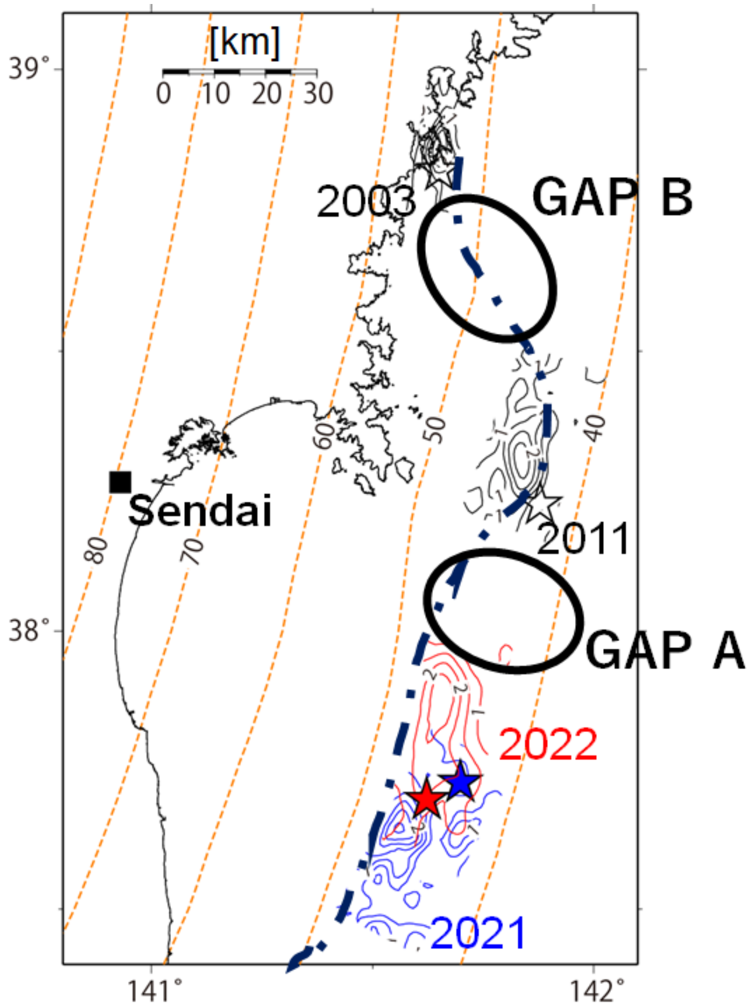

Figure 7: Surface projections of four DDC earthquakes in solid contours (intervals of 1 m), accompanied by the iso-depth contours of the plate boundary (dashed lines, Nakajima and Hasegawa, 2006). Note that the regions of high slip during the 2021 (denser blue contours) and 2022 (denser red contours) Fukushima-Oki earthquakes complement each other along the slab-strike direction.

Figure 8

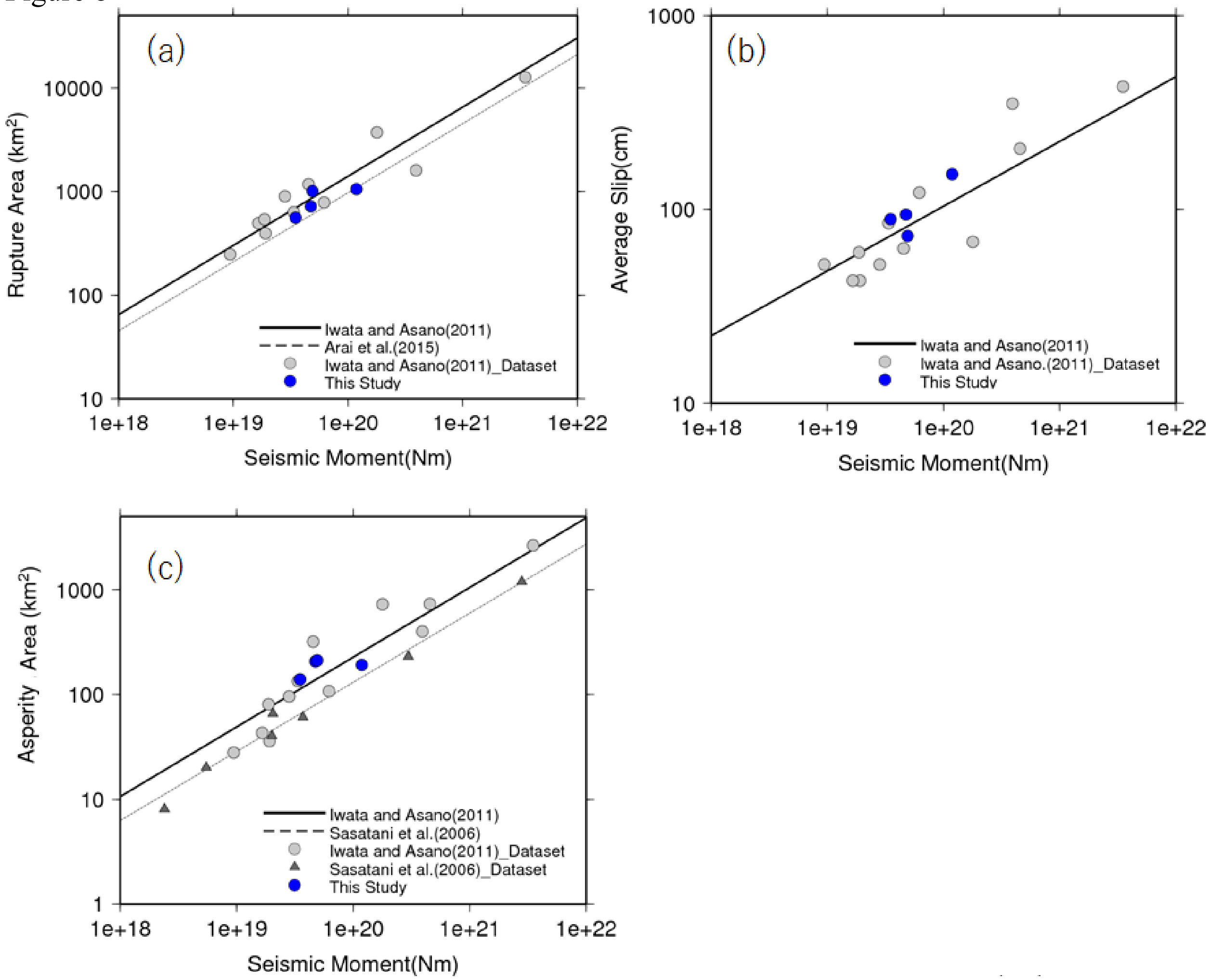

Figure 8: The moment dependency of rupture area (a), average fault slip (b), and asperity area (c) for intra-plate earthquakes. Empirical relations and data from three other studies (Sasataini *et al.*, 2006; Iwata and Asano, 2011 and Arai *et al.,* 2015) are included for comparison. See text for details.

Figure 9

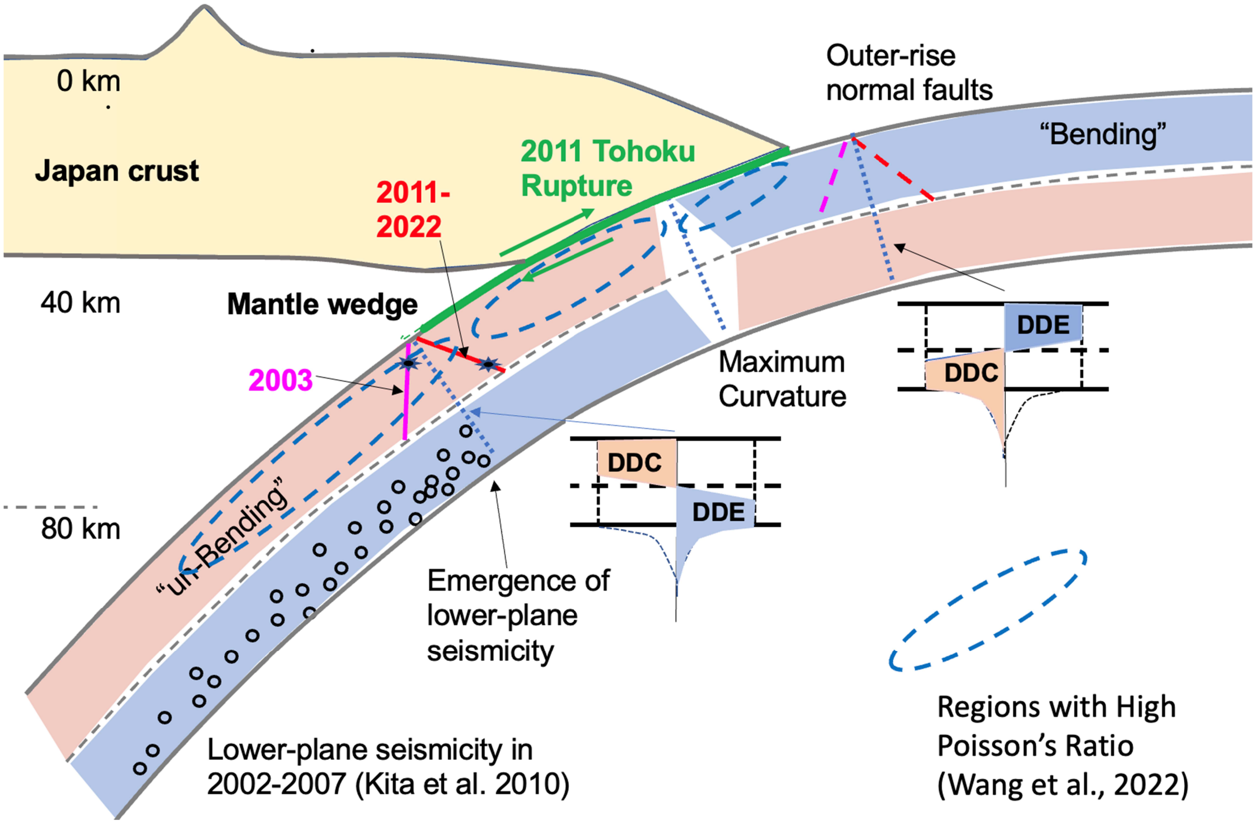

Figure 9: A 2D diagram of geometrical/mechanical concepts and observations used to constrain the observed intraslab earthquakes. Pink and blue colors are used to denote the compressional and extensional regions within the upper and lower plane of the subducted slab, which is separated by the neutral plane (black dashed line). The green line denotes the plate interface ruptured during the 2011 Mw 9 Tohoku earthquake. The magenta and red lines indicate the projections of the fault planes of these intraslab earthquakes. DDC and DDE denote the compression and extension along the slab's dip direction, respectively.

Table 1. Information of Mw 7 and larger earthquakes studied

Date	Hypocenter [*1]			M_W [*2]	Nodal Plane [*2] (Strike, Dip)	Slab Dip Angle [*3]
	Lat.	Lon.	Depth [km]			
2022/3/16	37.697°	141.623°	56.6	7.4	(15°, 43°)	18.5°
2021/2/13	37.729°	141.699°	55.4	7.1	(28°, 38°)	17.1°
2011/4/7	38.227°	141.879°	62.9	7.1	(20°, 40°)	17.5°
2003/5/26	38.821°	141.651°	62.0 [*4]	7.0	(190°, 69°)	26.9°
2021/3/20 [*5]	38.468°	141.628°	59.5	7.0	(192°, 17°)	16.5°

*1 Based on the JMA catalog
*2 Based on NIED (Fukuyama *et al.,* 1998)
*3 Estimated based on Nakajima and Hasegwa (2006)
*4 Based on waveform analysis for PS-time
*5 Interplate earthquake that we compared PGA (Figure 1 and Figure S1) with Intraslab earthquake

Table 2. Source parameters for each event

Date	Length*1 [km]	Width*1 [km]	M_O *2 [Nm]	Trimmed Fault Surface [km^2]	Average Slip*2 (After Trim) [m]	Weighted Slip Rate*2 [m/s]	$\triangle\sigma_S$ *2 [MPa]	$\triangle\sigma_{asperity}$ 2 [MPa]	$\triangle\sigma_E$ *3 [MPa]	E_R [J]	η_R
2022/3/16	44.0	28.0	1.08E+20	1232.0	1.60	1.17	6.08	16.07	11.24	9.60E+14	9.97E-02
2021/2/13	42.0	24.0	4.93E+19	880.0	0.76	1.03	4.60	21.99	16.14	3.26E+14	9.80E-02
2011/4/7	36.0	24.0	4.81E+19	720.0	0.95	1.18	6.07	19.32	14.55	2.23E+14	5.11E-02
2003/5/26	28.0	24.0	3.44E+19	560.0	0.89	0.80	6.32	14.31	11.60	5.28E+14	1.66E-01

*1 Based on the area of aftershock

*2 Resultant values estimated in this study

*3 Based on slip-weighted average (Noda *et al.,* 2013)

Table 3. Spatial correlations among fault slip, slip rate, and static stress drop

	2003	2011	2021	2022	Mean	1σ
$cor_{\Delta\sigma}^{D}$	0.85	0.82	0.85	0.90	0.86	0.034
cor_{T}^{D}	0.60	0.47	0.47	0.75	0.57	0.132
$cor_{\dot{D}}^{D}$	0.81	0.90	0.86	0.85	0.85	0.037
$cor_{\Delta\sigma}^{\dot{D}}$	0.69	0.78	0.78	0.76	0.75	0.042